

Dual-UWB Dielectric Resonator Antenna for OAM Communication

Zhe Wang^{*}, Haitao Nie, Shunshun Yue, Tailin Zhao, and Li Shi

Abstract—We designed a dielectric resonator antenna (DRA) that carries orbital angular momentum and has dual-band ultra-wideband characteristics based on the advantage of minor rain decay in L-band and C-band of microwave bands. The cavity of the antenna adopts an inner and outer nested spiral structure, and the material of resonant cavity shell is photosensitive resin. The internal medium is distilled water with a dielectric constant of 81, and the outer filling is saline with a concentration of 0.035 g/ml at room temperature for the dielectric constant. At the bottom of the cavity, we applied 2 feeds with phase difference of 90° to produce a circularly polarized beam in the DRA. Adjusting the size of the DRA and the height of the helical step surface to excite the OAM waves in higher order modes. The designed DRA generates resonance in 0.82–1.63 GHz and 3.35–7.27 GHz, and achieves ultra-wideband in both operating bands; furthermore, the antenna can generate OAM waves in $l = \pm 1$ and $l = \pm 3$ modes when operating at 1.51 GHz and 5.28 GHz, respectively. The simulation results match the measured results. The results show that the vortex wave generated by our designed antenna also has advantages such as high mode purity. Therefore, it can be effective in near-field communication and also provides a new solution for OAM near-field communication in 6G which is of great importance, and also for satellite communication and downlink signal transmission of communication satellites.

1. INTRODUCTION

Wireless communication is now in rapid development, and the arrival of the 5G era has intensified the intelligence of social development. In the context of the Internet of everything, the rapid growth of data traffic transmission brings a great challenge to the transmission quality and speed of wireless communication. The wireless communication by electromagnetic wave transmission is complete, and it carries angular momentum including spin angular momentum (SAM) and orbital angular momentum (OAM) [1]. Since the traditional modulation parameters based on time, frequency, polarization, and space are approaching the bottleneck in solving practical problems in communication, scholars have proposed adopting OAM for wireless communication [2]. Compared with conventional planar electromagnetic waves, the most important feature of OAM is its spiral phase and circular intensity distribution, so wireless communication using vortex electromagnetic waves can transmit the amplitude information of planar electromagnetic waves and phase information of OAM. The modes of OAM can theoretically take infinitely many values, and the beams between different modes are orthogonal to each other, which makes it possible to use for multiplexing and demultiplexing, thus increasing the channel capacity without relying on traditional resources such as time and frequency. OAM transmission at ultra-wideband (UWB) has many advantages, including high-speed transmission, low latency, high interference immunity, high reliability, high bandwidth, low power consumption, and no interference with other wireless signals [3]. These characteristics make UWB technology an ideal choice for future OAM communications. In recent years, many researchers have been designing single-mode or multi-mode OAM antennas. In 2012, Tamburini et al. [4] obtained an antenna that produces beams with phase

Received 29 May 2023, Accepted 17 August 2023, Scheduled 25 August 2023

^{*} Corresponding author: Zhe Wang (wangz0203@stu.xupt.edu.cn).

The authors are with Xi'an University of Posts & Telecommunications, China.

differences by cropping and distorting the reflecting surface of the antenna, to realize the generation of vortex electromagnetic waves. The generation of OAM waves by a metasurface antenna array is also one of the recent hot topics of research. In 2023, Yu's team proposed a transmissive meta-surface antenna based on the Pancharatnam-Berry phase arrangement for converting circularly polarized beams into multimode OAM beams with high polarization conversion rate and transmission efficiency [5]. A circular antenna array that can generate OAM beams is designed using eight Vivaldi elements connected in [6]. The feed is added to each cell so that each antenna cell has a continuous equal amplitude phase difference, and the phase difference between cells is 45° . By varying the order of phase difference $0, \pm 45^\circ, \pm 90^\circ, \pm 135^\circ$, and 180° , OAM beams with modes $0, \pm 1, \pm 2, \pm 3$, and 4 can be generated. Among various contemporary orbital angular momentum beam generation methods, the excitation of OAM waves by dielectric resonators is the hot spot and future development trend of research in related fields in recent years. The results of this study show that the cylindrical dielectric resonator antenna (CDRA) with solid state dielectric has good transmission characteristics and can also generate multi-mode OAM to improve the transmission efficiency [7]. A research team from City University of Hong Kong [8] designed a hemispherical DRA to excite $l = \pm 1$ and ± 2 mode OAMs by two orthogonal signal feeds.

In this paper, we design a DRA to generate OAM modes $\pm 1, \pm 3$ through such transmission phase structure on a helical step surface, and a stack of dielectric materials with different dielectric constants is used to achieve dual frequencies as well as UWB characteristics through resonance. The experimental measurements verify the performance of the OAM waves generated by the DRA, and the OAM purity is also analyzed and calculated. The structure of this letter is as follows. Section 2 shows the DRA structure's design and the simulation results' analysis. Section 3 offers the study of the actual measurement data of the proposed DRA. Section 4 provides the conclusion.

2. DESIGN AND ANALYSIS OF DRA

Figure 1 gives the model of proposed DRA. The cavity of the antenna has an inner and outer nested spiral structure, and the shell adopts photosensitive resin with a dielectric constant of 2.2 and a loss angle tangent of 0.01. The interior of the resonant cavity is full of distilled water with a dielectric constant of 81, and the exterior with saline with a concentration of 0.035 g/ml at room temperature has a dielectric constant of 93. The dielectric substrate uses FR4 material with a relative permittivity of 4.4 and a loss angle tangent of 0.02. The feed method differs from the commonly used microstrip line feed in a probe with a 90° difference at the bottom. The advantage of this feeding method is the ports at any position on the bottom to achieve impedance matching of the DRA. The Gaussian signal fed into the DRA through the probe has a phase difference of 90° , which can excite a circularly polarized electromagnetic wave, and the wave range difference generated when the circularly polarized wave passes through the spiral step surface adds phase information to it to turn it into multi-mode OAM waves with spiral phase. Finally, we obtained the final size of the DRA by using HFSS simulation software to optimize the DRA for a given dielectric constant, adjusting r_1, r_2 and the internal resonant cavity radius r , as shown in Table 1.

Table 1. Dimensions of the proposed antenna.

Parameter	Value (mm)	Parameter	Value (mm)
r_1	21.60	H	45.00
r_2	23.00	l_{sub}	60.00
r	8.00	d_{port}	20.00
h	7.00		

2.1. Process of DRA Design

By improving the DRA structure and finalizing the model, Fig. 2 shows the design process of the proposed antenna structure. The designed DRA in step 1 is a single spiral DRA filled with saline at

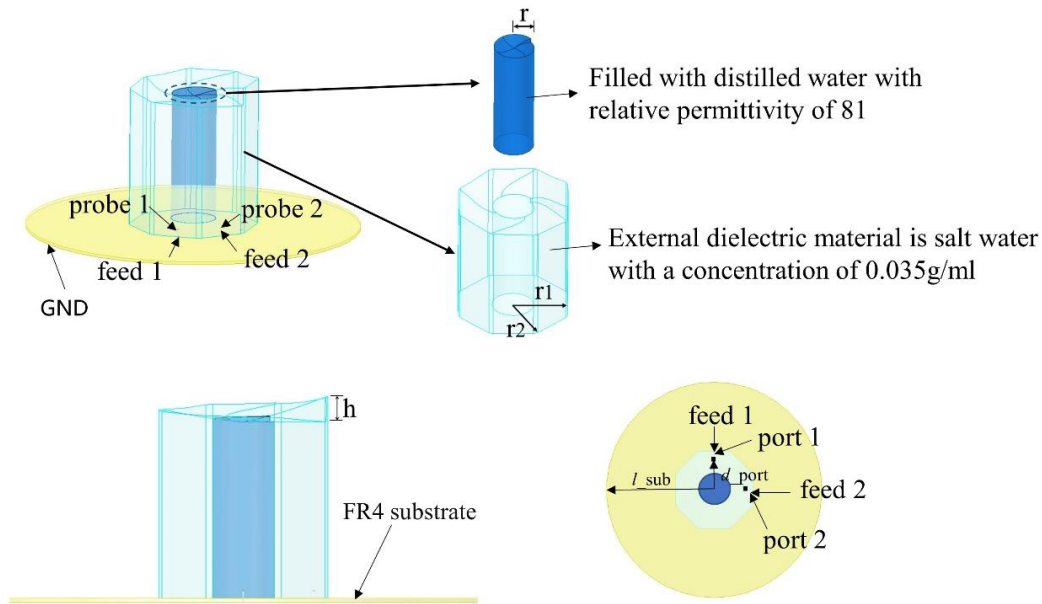


Figure 1. The model of proposed DRA.

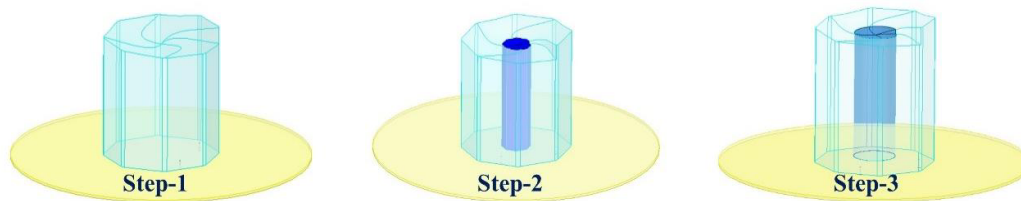


Figure 2. Different steps of DRA design.

a concentration of 0.035 g/ml at room temperature inside a photosensitive resin material shell, which eventually achieves dual-band narrowband performance. Since narrow-band transmission reduces the transmission speed and data capacity of the signal, limiting the number of OAM modes that can be transmitted as well as problems that can lead to the proliferation of OAM signals and reduce the quality and reliability of the signal, and the designed DRA needs to be improved to increase the operating bandwidth. In step 2, we inserted an octagonal spiral resonator in DRA, and the difference between the external medium is that the internal medium is distilled water with a dielectric constant of 81. The ultra-wideband characteristics of the designed antenna are achieved by the resonance of the two dielectric materials in the similar frequency band [9]. By modifying the DRA model and dimensional optimization calculation to make it have good impedance matching in the operating band, step 3 shows the final model.

2.2. Antenna Simulation Results

Reflection coefficient (S_{11}) and port isolation (S_{12}) for each step of the DRA design process by HFSS simulation software are shown in Figs. 3(a) and (b). The designed DRA works at 0.82–1.63 GHz and 3.35–7.27 GHz, achieving the dual-band ultra-wideband characteristics by generating 65.4% and 73.82% relative bandwidths in the two operating bands, respectively. The interposing of dielectric materials with different dielectric constants has a good bandwidth extension effect for the designed DRA. The isolation between the two orthogonal ports is less than -20 dB at the center frequency point, and the coupling between the ports hardly degrades the performance of the antenna, and it can work properly.

We can determine the number of OAM modes by adjusting the h of spiral step surface in the DRA

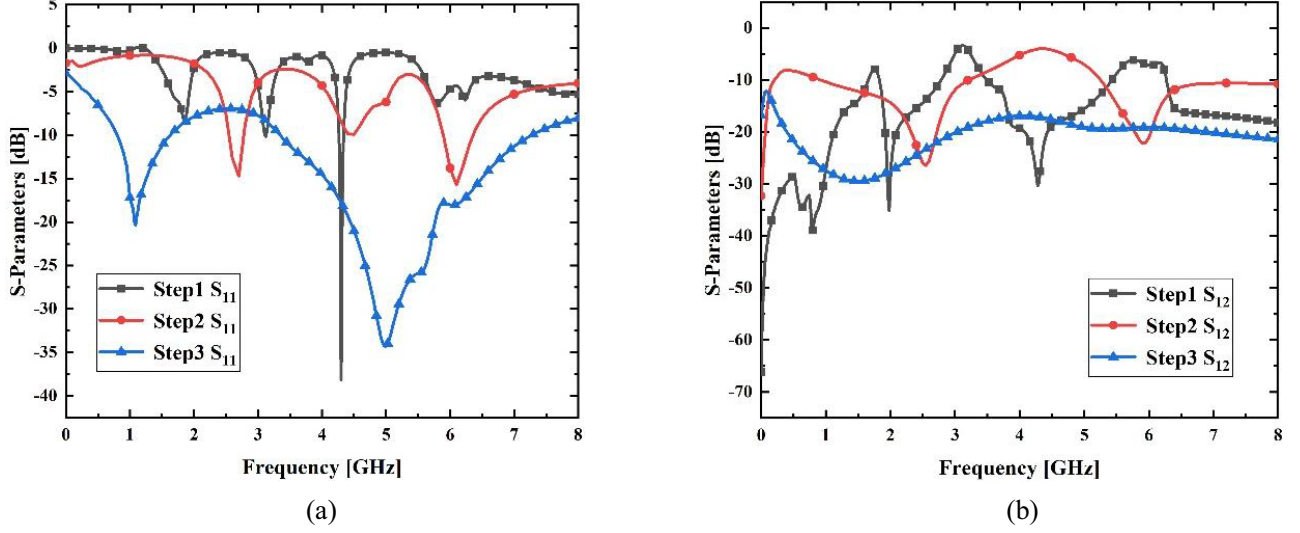


Figure 3. S -parameters of DRA for different steps. (a) S_{11} for different steps. (b) S_{12} for different steps.

as follows [10]:

$$\frac{l}{l+1} = \frac{7h}{2\lambda} \quad (1)$$

We can observe the phase distribution and magnitude of the electric field intensity of the proposed DRA by placing a circular observation plane at 120 mm from the top of the DRA. As shown in Fig. 1, our proposed DRA is a nested model, and the size of the antenna radius of the dielectric resonator inside determines the volume of two liquids with different dielectric constants. The second resonance between these two liquids has a non-negligible effect on the generated OAM electromagnetic vortex waves. We only consider feed ports with a phase difference of 90° in simulation, and there are multiple OAM modes generated when the radius r of the inner cavity is 6 mm, 8 mm, and 10 mm, respectively, as shown in Table 2.

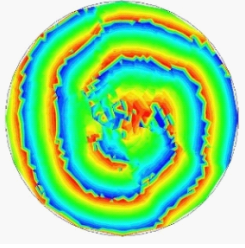
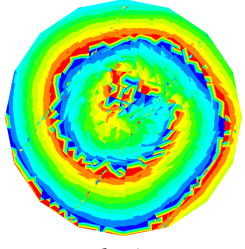
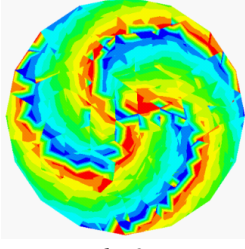
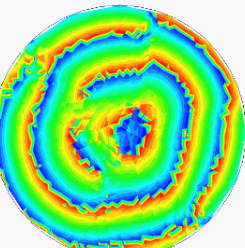
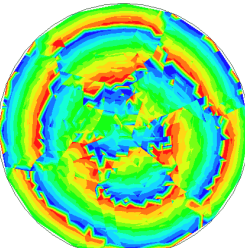
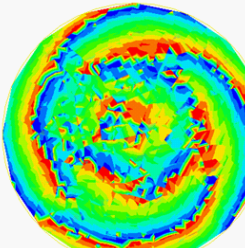
Table 2 shows that when radius r is 6 mm and 10 mm, the resulting OAM phases all produce non-negligible aberrations, seriously lowering the OAM communication quality. When r is 8 mm, the OAM phases of $l = +1$ and $l = +3$ modes are clear and have obvious vortex wave phase characteristics.

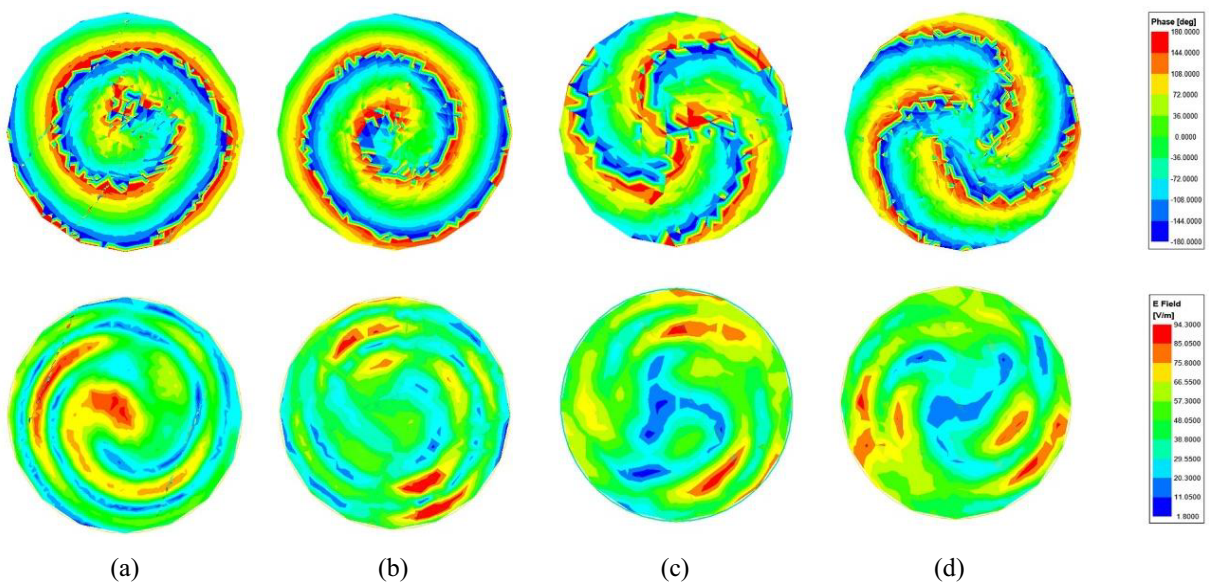
Figure 4 shows the modes of the OAM wave at different frequencies and their electric field distributions when r is 8 mm. When the phase difference before the two feed ports is $+90^\circ$, we observe the $l = +1$ mode as shown in Fig. 4(a) from the observation window at 1.51 GHz, with a clockwise spiral arm in the OAM phase diagram. By changing the phase difference between the ports to -90° , the OAM phase diagram changes to a counterclockwise single spiral arm with $l = -1$ mode as shown in Fig. 4(b). At 5.28 GHz, the OAM phase becomes a clockwise triple spiral arm, a typical $l = +3$ mode of the OAM wave as shown in Fig. 4(c). Similarly, when the phase difference is changed between the ports to -90° , the OAM wave of $l = -3$ mode will be generated as shown in Fig. 4(d).

3. ANTENNA MEASUREMENT RESULTS AND ANALYSIS

Through optimization, we finally chose the dimensions shown in Table 1 for the DRA prototype fabrication. We produced the spiral shell of the DRA through 3D printing, then distilled water and saline with a concentration of 0.035 g/ml into the inside and outside of the DRA, by injecting through a syringe, respectively. The probes were connected to the chamber through the dielectric substrate and glued to the substrate, and finally the probes were soldered to the copper-clad surface to complete the DRA prototype. Its structure is as shown in Figs. 5(a)–5(c), and we measured the DRA in an anechoic chamber for near-field testing as shown in Fig. 5(d).

Table 2. OAM phase distribution for different values of r .

r/mm	OAM Phase Distribution		
6	 $l = 2$		
8	 $l = 1$	 $l = 3$	
10	 $l = 1$	 $l = 3$	 $l = 4$

**Figure 4.** Phase distribution and electric field magnitude of the DRA at 1.51 GHz and 4.28 GHz. (a) When $l = +1$. (b) When $l = -1$. (c) When $l = +3$. (d) When $l = -3$.

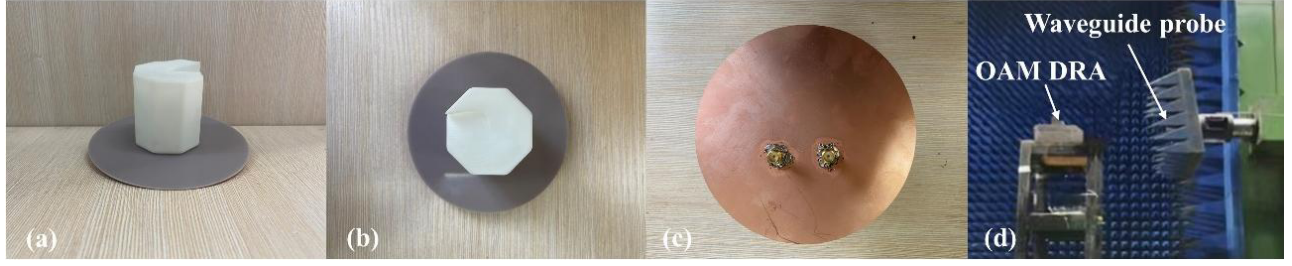


Figure 5. 3D printed DRA prototype and test environment. (a) DRA prototype. (b) Top view of DRA. (c) Bottom feed of the substrate. (d) Measurements of the anechoic chamber environment.

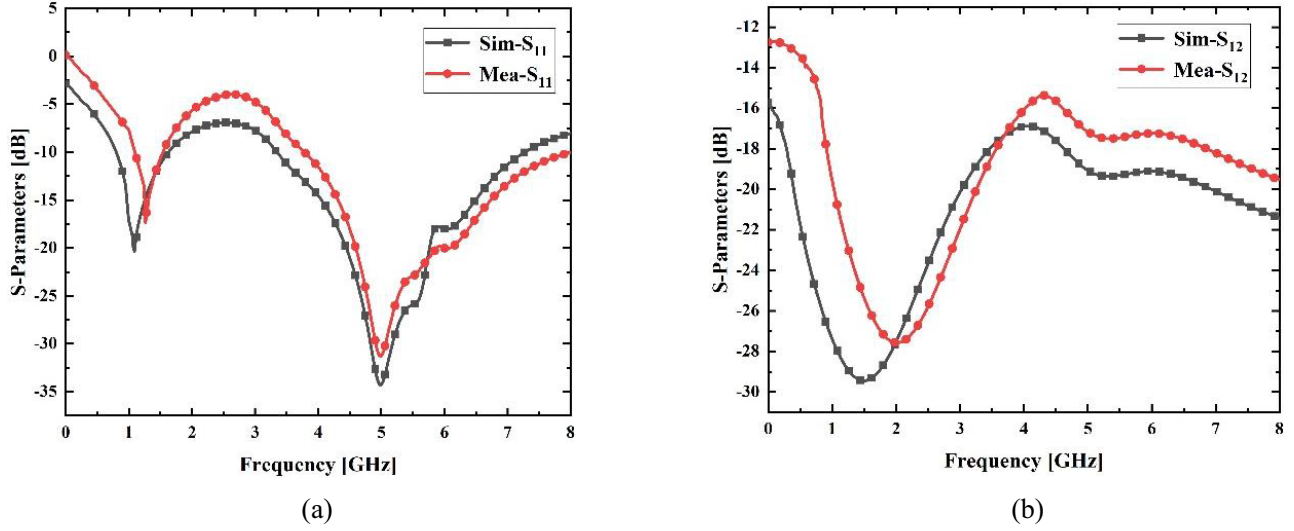


Figure 6. Comparison of actual measurement and simulation results of S -parameters of the DRA prototype. (a) Actual measurement and simulation results of S_{11} . (b) Actual measurement and simulation results of S_{12} .

The S -parameter plots of the simulated and measured DRAs are in Fig. 6 by actual measurement of the DRA performance. The measured antenna impedance bandwidth and isolation between the ports match well with the simulated results. The deviation of the results may be caused by improper soldering at the feed of the DRA during the assembly.

We used the OAM probe in the near-field anechoic chamber for data acquisition of the DRA and obtained the OAM transmission data in different modes. Fig. 7 plots the OAM phase distribution and electric field distribution for the $l = \pm 1$ and $l = \pm 3$ modes by MATLAB.

In addition, we also calculated the OAM purity in different modes. In the transmitted amplitude field, extract the toroidal electric field around the null-amplitude point separately for Fourier transform analysis [11].

$$A_l = \frac{1}{2\pi} \int_0^{2\pi} \psi(\varphi) d\varphi e^{-jl\varphi} \quad (2)$$

$$\psi(\varphi) = \sum_l A_l e^{jl\varphi} \quad (3)$$

where $\psi(\varphi)$ is a function of the sampling field, and A_l is the amplitude of the corresponding mode. The ratio of each mode component to the total energy can indicate the purity of the OAM. Fig. 8 shows the purity energy weights of different OAM modes, which account for 80.3% of the simulated

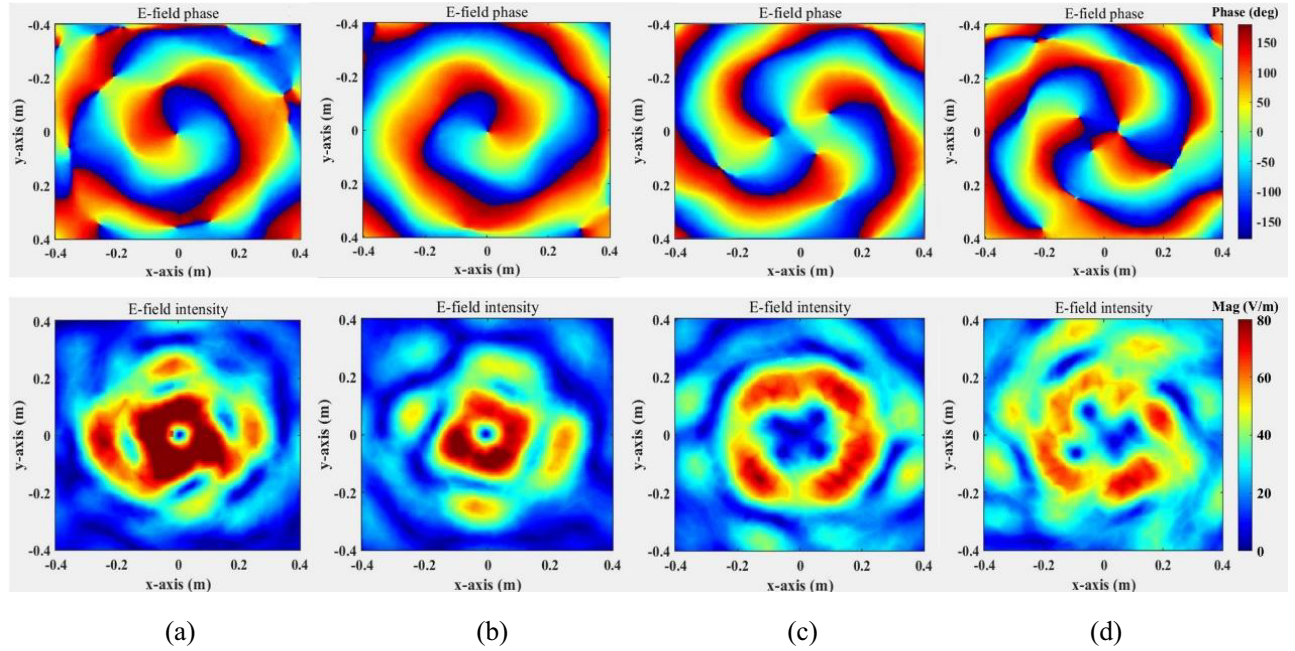
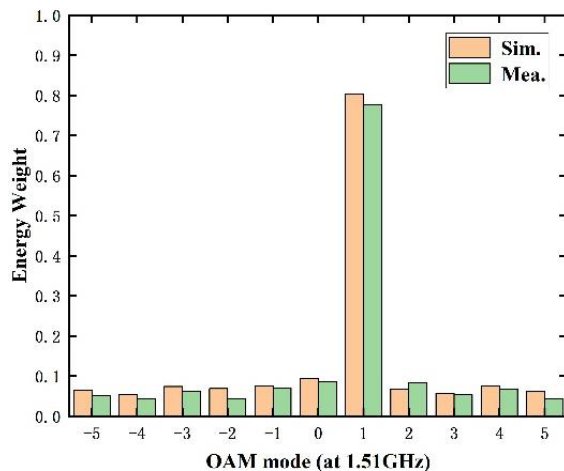


Figure 7. Measured phase and electric field distribution. (a) $l = +1$. (b) $l = -1$. (c) $l = +3$. (d) $l = -3$.

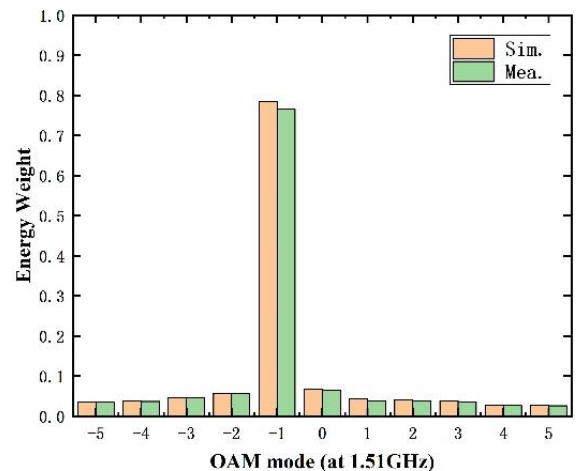
purity at $l = +1$ (77.6% measured), 78.4% of the simulated purity at $l = -1$ (76.5% measured), 77.5% of the simulated purity at $l = +3$ (75.3% measured), and 78.2% of the simulated purity at $l = -3$ (74.7% measured). The primary mode energy is much larger than the other modes, and the inter-mode interference is negligible. The proposed antenna has high mode purity for different modes of transmission and can perform high quality wireless communication.

Finally, we measured the two-dimensional radiation directional plots when the DRA generated OAM waves. Fig. 9 gives the direction diagrams in the E -plane and H -plane when the DRA operates at 1.51 GHz and 5.28 GHz, with typical OAM direction diagram center depression characteristics. The measured and simulated results are consistent, so our proposed antenna can effectively transmit OAM signals.

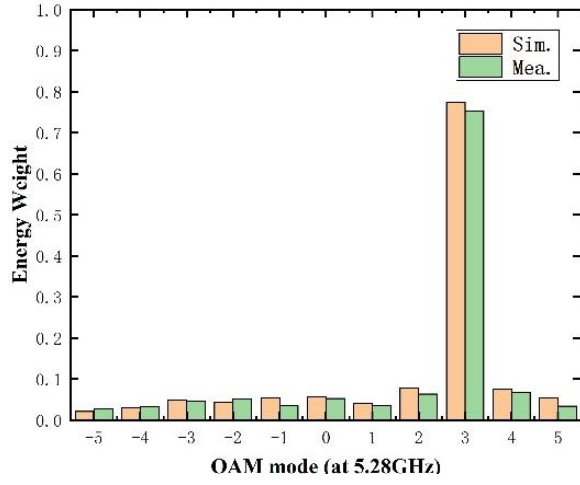
To visualize the advantages of the proposed DRA in wireless communication, Table 3 compares this scheme and the currently available OAM antennas.



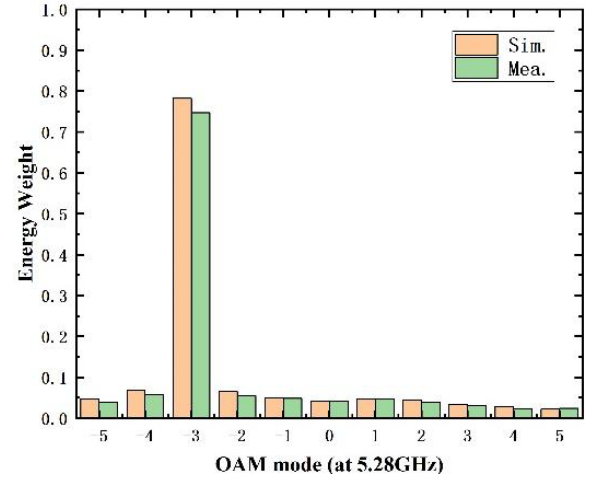
(a)



(b)

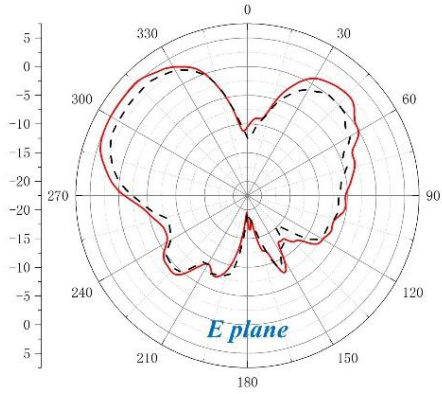


(c)

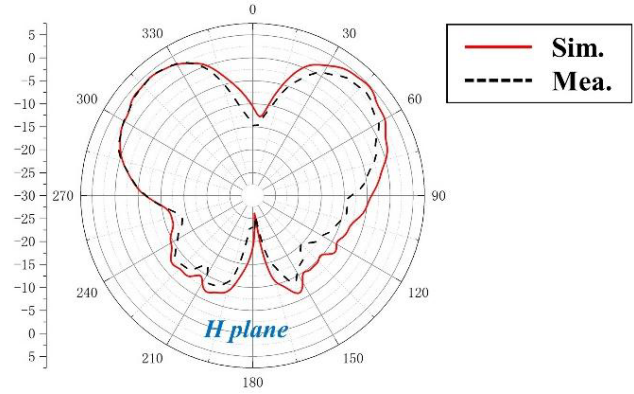


(d)

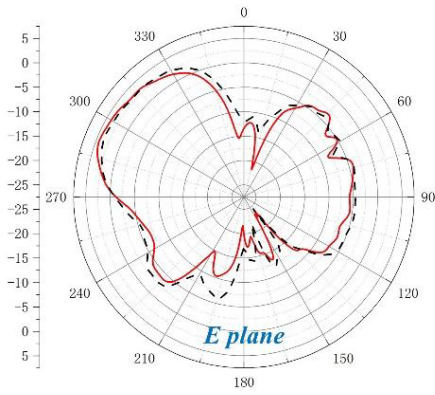
Figure 8. OAM model purity. (a) When $l = +1$. (b) When $l = -1$. (c) When $l = +3$. (d) When $l = -3$.



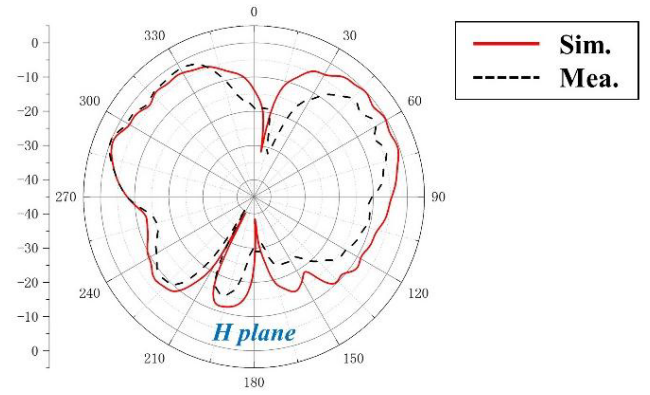
(a)



(b)



(c)



(d)

Figure 9. 2-D radiation patterns of the DRA. (a) E plane at 1.51 GHz. (b) H plane at 1.51 GHz. (c) E plane at 5.28 GHz. (d) H plane at 5.28 GHz.

Table 3. Performance comparison between the designed DRA and the currently available OAM antennas.

Ref.	Antenna Type	Frequency Bands (GHz)	OAM modes	Bandwidth	OAM Purity (%)
[12]	DRA	1.60 GHz & 5.10 GHz	± 1 , ± 3	400 MHz & 740 MHz	-
[13]	3D helical antenna	1.55 GHz, 2.45 GHz	+1, +2	Nearly 167 MHz & 83 MHz & 125 MHz	Nearly 80.00%
[14]	Cross-dipole antenna array	2.05–4.11 GHz	+1	66.90%	35.00%–60.00%
[15]	Meta-surface Antenna	4.90 ~ 6.50 GHz & 5.00 ~ 6.30 GHz	± 1	28.10% & 24.60%	64.80%, 63.60%
Prop.	DRA	0.82–1.63 & 3.35–7.27 GHz	± 1 , ± 3	65.40% & 73.82%	80.30%

4. CONCLUSION

In this paper, we propose a dual-band UWB DRA that covers L-band and C-band of the microwave frequency band, excites circularly polarized wave by inputting orthogonal Gaussian signals from two SMA probes at the bottom with a 90° difference, and generates OAM beams by attaching a phase factor to the circularly polarized wave through the spiral surface at the top of the DRA. Adjusting the height h of the spiral surface can excite different modes of OAM waves. To verify the simulation results, the DRA prototypes with $r_1 = 21.6$ mm, $r_2 = 23$ mm, and $r = 8$ mm were assembled and measured in an anechoic chamber. The measurement results show that the proposed double spiral DRA can generate two UWB working bands with relative bandwidths of 65.4% and 73.82%, and generate OAM waves with $l = \pm 1$ mode at 1.51 GHz and $l = \pm 3$ mode at 5.28 GHz, and its mode purity measured results are higher than 74%, which can realize high purity and high quality OAM. The wireless communication not only provides a new solution for future 6G communication, but also has essential significance for satellite communication and downlink signal transmission of communication satellites.

REFERENCES

- Allen, L., M. W. Beijersbergen, R. J. C. Spreeuw, and J. P. Woerdman, "Orbital angular momentum of light and the transformation of Laguerre-Gaussian laser modes," *Physical review. A, Atomic, Molecular, and Optical Physics*, Vol. 45, No. 11, 8185–8189, 1992 (in English).
- Thide, B., et al., "Utilization of photon orbital angular momentum in the low-frequency radio domain," *Physical Review Letters*, Vol. 99, No. 8, 087701, 2007 (in English).
- Wang, Y., X. Sun, and L. Liu, "A concentric array for generating multimode OAM waves," *Journal of Communications and Information Networks*, Vol. 7, No. 3, 324–332, 2022.
- Tamburini, F., E. Mari, A. Sponselli, B. Thidé, A. Bianchini, and F. Romanato, "Encoding many channels on the same frequency through radio vorticity: First experimental test," *New Journal of Physics*, Vol. 14, No. 3, 033001, 2012.
- Yu, Z., L. Shi, and Z. Xin, "Polarization conversion and OAM generation with a single transmitting metasurface," *Progress In Electromagnetics Research M*, Vol. 115, 129–140, 2023.
- Deng, C. J., W. H. Chen, Z. J. Zhang, Y. Li, and Z. H. Feng, "Generation of OAM radio waves using circular vivaldi antenna array," *International Journal of Antennas and Propagation*, Vol. 2013, Art. No. 847859, 2013.

7. Liang, J. and S. Zhang, "Orbital Angular Momentum (OAM) generation by cylinder dielectric resonator antenna for future wireless communications," *IEEE Access*, Vol. 14, No. 8, 9570–9574, Aug. 2016.
8. Ren, J. and K. W. Leung, "Generation of microwave orbital angular momentum states using hemispherical dielectric resonator antenna," *Applied Physics Letters*, Vol. 112, No. 13, 131103, Mar. 2018.
9. Aayesha, M. B. Q., M. Afzaal, M. Shuaib Qureshi, and J. Gwak, "Ultra-wideband annular ring fed rectangular dielectric resonator antenna for millimeter wave 5G applications," *Computers, Materials & Continua*, Vol. 71, No. 1, 1331–1348, 2022.
10. Singh, R. P. and P. G. Poonacha, "Survey of techniques for achieving topological diversity," *IEEE Communications*, 1–5, 2013.
11. Jack, B., M. J. Padgett, and S. Franke-Arnold, "Angular diffraction," *New Journal of Physics*, Vol. 10, No. 10, 103013, 2008.
12. Yu, Z., Q. Gao, B. He, and L. Guo, "Effects of concentration, temperature and geometry on double spiral liquid orbital angular momentum antenna," *IEEE Antennas and Wireless Propagation Letters*, 1–1, 2021.
13. Shen, F., J. Mu, K. Guo, S. Wang, and Z. Guo, "Generation of continuously variable-mode vortex electromagnetic waves with three-dimensional helical antenna," *IEEE Antennas and Wireless Propagation Letters*, Vol. 18, No. 6, 1091–1095, 2019.
14. Yang, Z., J. Zhou, L. Kang, B. Liu, G. Yang, and X. Shi, "A closed-loop cross-dipole antenna array for wideband OAM communication," *IEEE Antennas and Wireless Propagation Letters*, Vol. 19, No. 12, 2492–2496, 2020.
15. Wu, J., Z. X. Zhang, X. G. Ren, Z. X. Huang, and X. L. Wu, "A broadband electronically mode-reconfigurable orbital angular momentum metasurface antenna," *IEEE Antennas and Wireless Propagation Letters*, Vol. 18, No. 7, 1482–1486, 2019.